DEUTSCHES ELEKTRONEN-SYNCHROTRON

DESY 93-097
July 1993

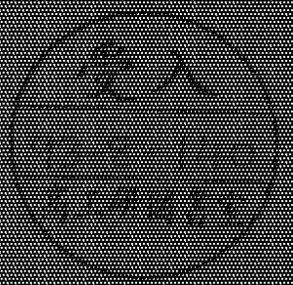

Deep Inelastic Scattering at Low-x Results from the H1 Experiment

S. Levonian

Deutsches Elektronen-Synchrotron DESY, Hamburg

ISSN 0418-9833

NOTKESTRASSE 85 — 22603 HAMBURG

Diese Seite enthält Daten, die nicht zum Download angeboten werden.
Weitere Informationen finden Sie auf unserer Internetseite.

Diese Seite enthält Daten, die nicht zum Download angeboten werden.
Weitere Informationen finden Sie auf unserer Internetseite.

This page contains data not available for download.
Please visit our website for more information.

This page contains data not available for download.
Please visit our website for more information.

DESY
Bibliothek
Notkestraße 85
22607 Hamburg
Germany

DESY-IfH
Bibliothek
Platanenallee 6
15738 Zeuthen
Germany

DESY 93-087
July 1993

ISSN 0418-9833

Deep Inelastic Scattering at Low-x Results from the H1 Experiment *

Albert De Roeck
Deutsches Elektronen Synchrotron "
D-2000 Hamburg 52, Notkestrasse 85, Germany

for the

H1 Collaboration

ABSTRACT

We present new results from the H1 experiment on deep inelastic ep scattering at HERA. The results are based on the complete data sample of 1992, corresponding to an integrated luminosity of 23 nb^{-1}. Particle energy flow, transverse momentum characteristics and jet rates have been measured for the hadronic final state. QCD based models with different assumptions concerning initial and final state parton emission have been compared with the data. The first measurement of the $F_2(x,Q^2)$ structure function for Bjorken-x values down to $x = 4.10^{-4}$ and $Q^2 > 10$ GeV^2 is presented. The preliminary results show a rather steep rise of the structure function at small x.

* Invited Talk presented at the Durham Workshop "HERA the new frontier for QCD, Durham, UK, March 1993"

1 Introduction

High energy deep inelastic lepton nucleon scattering has long been recognized to be an important testing ground for our understanding of matter. About 25 years ago, pioneering experiments[1] discovered the partons in nucleons. Since then deep inelastic lepton scattering experiments [2, 3] have provided important information on the structure of the proton and on the nature of the interactions between leptons and quarks. The electron proton collider HERA, in which 26.7 GeV electrons collide with 820 GeV protons, allows the extension of this line of research into as yet unexplored kinematic regions; down to very small Bjorken-x values and up to very large four-momentum transfer squared Q^2.

This paper describes new analyses of the neutral current deep inelastic scattering (DIS) data collected with the H1 detector [4] in 1992, the first year of data taking at HERA. The total integrated luminosity usable for DIS analyses amounts to 23 nb^{-1}. Studies of the hadronic final state and a first preliminary measurement of the structure function $F_2(x,Q^2)$ are presented.

The kinematics of the inclusive deep inelastic scattering process $ep \to eX$ at fixed centre of mass energy, $\sqrt{s}$, is determined by two independent variables, conventionally chosen to be two of x, y and Q^2. The H1 experiment at HERA measures both the scattered electron and the hadronic final state produced between the struck quark and the proton remnant, thus the collision kinematics can be determined from electron variables, hadronic variables or a mixture of both.

The kinematical variables are defined as follows:

$$Q^2 = -q^2 = -(p_e - p_l)^2, \quad x = \frac{Q^2}{2P.q}, \quad y = \frac{P.q}{P.p_e}, \quad W^2 = (q+P)^2 = Q^2\frac{1-x}{x} + {m_p}^2, \qquad (1)$$

where Q^2 is the four-momentum transfer squared, x the momentum fraction of the proton carried by the struck parton, y the fraction of the energy transfer in the proton rest system, and W^2 the hadronic invariant mass squared. In these definitions p_e, p_l and P denote the four momenta of the incoming and scattered lepton and the incoming proton respectively; m_p is the mass of the proton. At HERA the centre of mass energy squared $s = 4E_eE_p = 87\,600$ GeV^2, with E_e and E_p the energy of the incoming electron and proton respectively. Since $Q^2 = xys$, x values down to $\sim 10^{-4}$ in the deep inelastic regime can be accessed at HERA.

The kinematic variables in charged lepton nucleon scattering are traditionally determined from the angle, θ_e, and the energy of the scattered lepton, E'_e, through the relations

$$Q^2 = 4E_eE'_e\cos^2(\theta_e/2), \quad y = 1 - (E'_e/E_e)\sin^2(\theta_e/2) \text{ and } x = Q^2/(sy) \qquad (2)$$

Polar angles are measured relative to the proton beam direction, termed the forward direction in the following. The kinematics for the scattered electron is shown in Fig. 1a. It follows that for a large region at low Q^2, namely for $y < 0.1$, the energy of the scattered electron is close to the incident electron beam energy. This results in a peak in the electron energy spectrum –termed the kinematic peak – which is useful for calibration purposes. Fig. 1b shows the distribution of the deep inelastic event candidates in the x and Q^2 plane. These events were selected by requiring an electron candidate with an energy of at least 8 GeV in the detector, using very loose electron identification criteria. No attempt was made to remove residual background for this plot. Most data are accumulated at low Q^2 and low x, resulting from the $1/Q^4x$ dependence of the cross section (eqn.(4) see below). The resolution in Q^2, when determined according to eqn.(2), is dominated by the electron energy resolution. Therefore this determination of Q^2 is superior to others based on the hadronic energy or angle measurement. This is not true for the variable y, which from the electrons alone can not be accurately determined below $y \leq 0.05$ as the resolution of such a determination varies like $1/y$.

A second method of determining the kinematics uses the definition of y with the hadronic final state measurement which allows to access the lower y or larger x region. The hadronic y variable is determined using the relation [5]

$$y_h = \sum_{hadrons} \frac{E_h - p_{z,h}}{2E_e} \qquad (3)$$

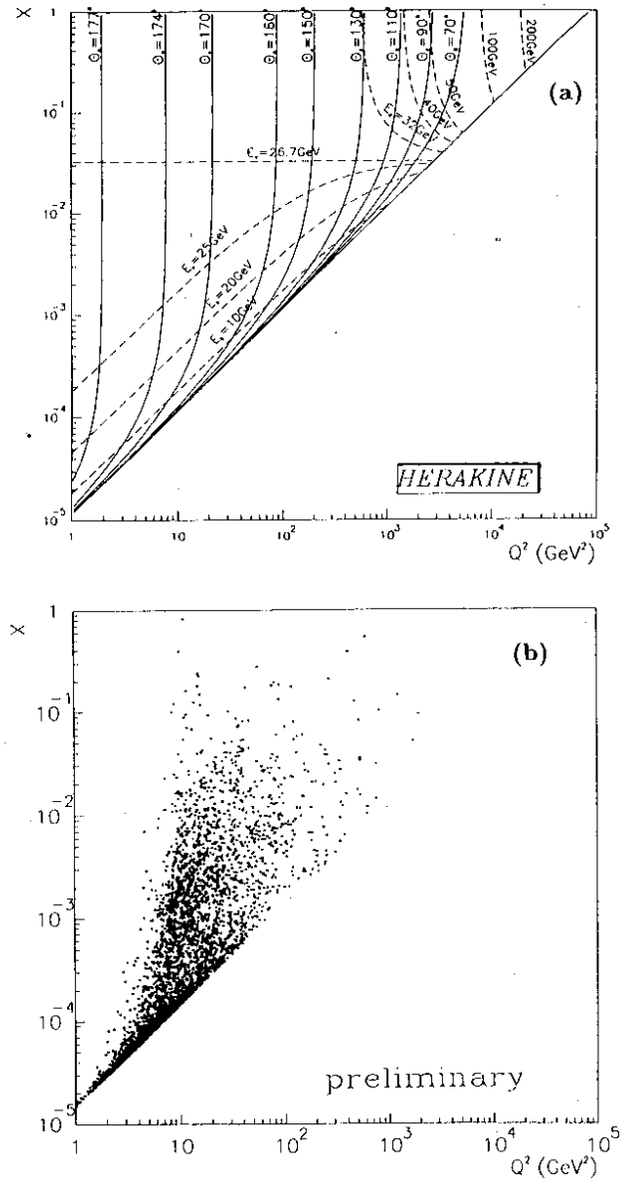

Figure 1: **(a)** *iso-angular and iso-energy lines of the scattered lepton in the kinematic $x - Q^2$ plane at HERA.* **(b)** *distribution of the DIS event candidates for $y < 0.7$ in the $x - Q^2$ plane.*

where E_h is the energy of a hadron and p_z its momentum component along the $+z$ direction.

For the hadronic final state analysis (section 3) y_h is used to determine the kinematics, while for the structure function analysis (section 4) the results derived with y_e and y_h are compared.

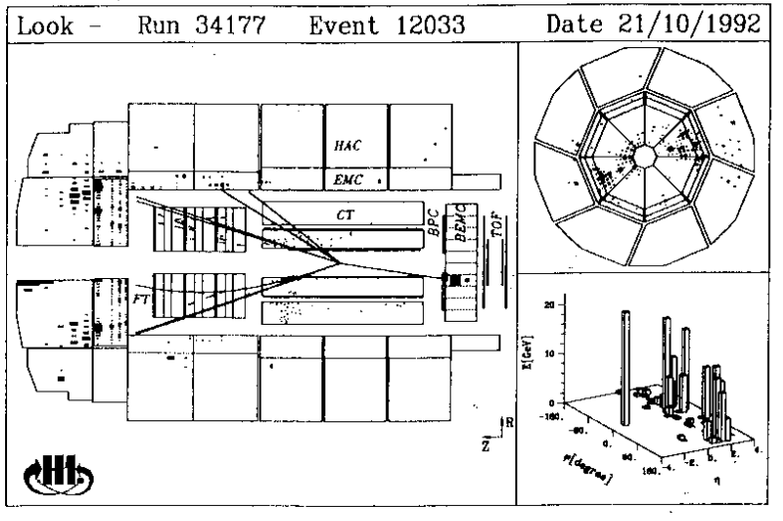

Figure 2: *A deep inelastic scattering event at $x = 0.0012$ and $Q^2 = 15$ GeV^2, observed in the H1 detector. The detector components shown are: the electromagnetic (EMC), hadronic (HAC) and backward electromagnetic (BEMC) calorimeters, forward (FT) and central (CT) trackers, backward proportional chamber (BPC), and scintillator hodoscope (TOF).*

2 The H1 Experiment

A detailed description of the H1 detector can be found in [4].

Fig. 2 shows a deep inelastic scattering event at $x = 0.0012$ and $Q^2 = 15$ GeV^2, which are typical values for the present data sample, observed in the H1 detector. Most of the detector components important for the analyses described here are visible. These are:

- The tracker: the central tracking detector consists of two large jet drift chamber modules, two z drift chambers and two multiwire proportional chambers for triggering. Its angular acceptance is $15^0 - 170^0$. The forward tracking detector accepts tracks between 7^0 and 25^0. It consists of three modules of drift and multiwire proportional chambers. The backward multiwire proportional chamber (BPC) has 4 wire planes and an angular acceptance of $155^0 - 175^0$. A superconducting coil provides a uniform magnetic field of 1.2 T in the tracking region.
- The calorimeters: the backward electromagnetic calorimeter (BEMC) is made of 88 lead/scintillator sandwich stacks, each with a depth of 22 radiation lengths, corresponding to about 1 interaction length, and transverse dimensions of 16 by 16 cm^2. The liquid argon (LAr) calorimeter consists

of an electromagnetic section with lead absorber (20 to 30 radiation lengths) and a hadronic section with steel absorber. The total depth of the calorimeter varies between 4.5 and 8 interaction lengths.

- The time of flight (TOF) system, located behind the backward calorimeter, consists of two scintillator planes, each with a time resolution of about 3 ns, and enables the separation of genuine ep events from proton beam-wall and beam-gas interactions upstream of the detector at the trigger level.

- The luminosity detector system described in [6], not visible in Fig. 2, is designed to detect the $e-\gamma$ coincidence from the reaction $e+p \rightarrow e+\gamma+p$. The electron tagger is located 33m from the interaction region in the backward, or $-z$, direction and detects electrons scattered through angles less than 5 mrad with respect to the electron beam direction. The photon tagger is located at $z=-103$m. Both detectors are TlCl/TlBr crystal calorimeters. The current uncertainty on the luminosity measurement amounts to 7%.

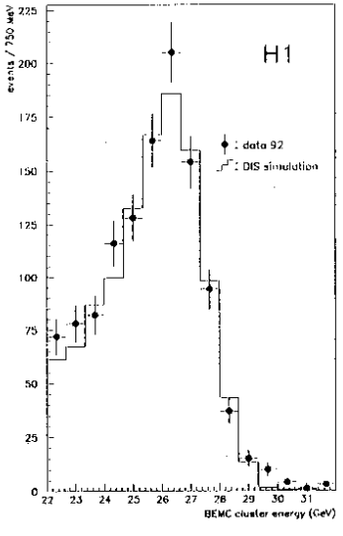

Figure 3: *Electron energy spectrum of the DIS events compared with a Monte Carlo simulation [7, 8] of the H1 detector using the parametrization MRSD0 [9]. The simulated spectrum is normalized to the measured integrated luminosity of 23 nb^{-1}.*

From Fig. 1 it follows that for most of the DIS events the electron is scattered in the backward region and is detected in the BEMC, an understanding of which is therefore crucial for the presented analyses. Since knowledge of the absolute energy scale is extremely important for the precision of the reconstruction of y_e and Q^2, much care has gone into the analysis of the calibration of this detector. Fig. 3 shows the kinematic peak in the electron energy spectrum, for data compared with a Monte Carlo simulation. The peak position is only weakly dependent on the underlying, a priori unknown, cross section of the data and can thus conveniently be used to calibrate the energy scale of the detector. Using this calibration method the energy scale of the BEMC for electrons is currently known to better

than 2%. This method was cross checked by determining the electron energy from the angle of the electron and the current jet (see e.g. [10]).

The initial calibration of the LAr calorimeter was based on test beam measurements using electrons and pions at CERN. The absolute scale of the energy response at HERA has been verified with charged particles by comparing their momentum measured in the central tracker with associated energy deposited in the calorimeter. With electrons and positrons produced by cosmic ray muons, the electromagnetic scale has been checked to $\pm 2\%$ [11]. Using negatively charged particle tracks originating from the ep interaction region, the hadronic scale has been checked to $\pm 10\%$. Furthermore, a study of the balance of transverse momentum between the scattered electron measured in the backward calorimeter and the recoiling hadronic system measured in the LAr calorimeter demonstrates that the overall hadronic energy scale of the LAr calorimeter is understood to within $\pm 7\%$. All calibrations will improve as more data, allowing for more accurate studies, are accumulated.

For events with a large electron scattering angle θ_e the angle is determined by the vertex of the event and the reconstructed hit in the BPC. The angular resolution $\delta\theta_e$ depends only weakly on θ_e and is about 6 mrad. For events with $\theta_e < 157^0$, the electron scattering angle is determined from the vertex and tracks in the central tracking detector.

3 Hadronic Final States

Previous lower energy lepton-nucleon DIS measurements [12, 13, 14] have shown that the topological characteristics of the hadronic final state can only be described if QCD corrections are made to the naive parton model. In particular, the observed event shapes and the transverse momentum (p_T) distributions of final state hadrons were described in terms of $O(\alpha_s)$ QCD matrix elements, additional effects of soft gluons, and fragmentation [15].

In this section we study general characteristics of the hadronic final state, in terms of the energy flow as a function of pseudorapidity and azimuthal angle, and the average transverse momentum as a function of the variable Feynman-x, the so called seagull plot. Jet measurements and rates will be shown, using the JADE cluster algorithm. A first measurement of the hadronic final state in deep inelastic scattering of 26.7 GeV electrons and 820 GeV protons in the H1 experiment based on a data sample corresponding to an integrated luminosity of 1.6nb^{-1} is reported in [16]. The first H1 results on jets are also reported in [17]. First results from the ZEUS collaboration on hadronic final states are reported in[18].

3.1 Event Selection

Events are selected with an electromagnetic cluster in the BEMC or LAr calorimeter. We define a "low-Q^2" sample consisting of events which have the scattered electron in the backward calorimeter, ($157^\circ \lesssim \theta_e \lesssim 173^\circ$, 8 GeV$^2 \lesssim Q^2 \lesssim 100$ GeV^2), and a "high Q^2" sample consisting of events which have the electron scattered into the LAr calorimeter ($\theta_e \lesssim 155^\circ$, $Q^2 \gtrsim 100$ GeV^2). A cut on y is applied ($y < 0.5$ and $y < 0.6$ in the low and high Q^2 samples, respectively) in order to avoid regions in which QED corrections and residual photoproduction background may be large. A cut on the hadronic invariant mass ensures a substantial hadronic energy flow in the detector. For the energy flow and $< p_T >$ versus x_F study this cut amounts to $W^2 > 3000$ GeV^2, while for the jet analysis we have chosen $W^2 > 5000$ GeV^2. Characterisitics of the resulting data samples, with the larger W^2 cut, and their kinematic ranges are summarized in Table 1.

The distributions shown in this section are not corrected for detector acceptance and resolution. They are compared with model calculations including a full simulation of the H1 detector. The above cuts ensure that the influence of detector acceptance and resolution on the distributions studied is small. Further, it is important to note that in most figures in this section each event contributes to more than one data point; the datapoints are thus correlated.

	low Q^2, 1100 events		high Q^2, 64 events	
	mean	range	mean	range
x	$1.5 \cdot 10^{-3}$	$10^{-4} - 10^{-2}$	$3 \cdot 10^{-2}$	$10^{-3} - 10^{-1}$
Q^2 [GeV^2]	15	8 – 100	520	> 100
W [GeV]	90	70 – 210	130	70 – 230

Table 1: Kinematic properties of the data sample used in the jet analysis

3.2 QCD Models and Simulation

Three different prescriptions for the simulation of QCD effects in deep inelastic scattering are compared to our data:

- Quark parton model and leading log parton showers.
- $O(\alpha_s)$ matrix elements with matched parton showers.
- The colour dipole model.

The leading log parton shower models used are in LEPTO 5.2 [8], labelled PS, and HERWIG 5.5 [19], labelled HERWIG. For $O(\alpha_s)$ matrix elements with matched parton showers the model in LEPTO 6.1 [20], labelled ME+PS was used. Finally the colour dipole model calculations were obtained using ARIADNE 4.03 [21] (as implemented in LEPTO 6.1, i.e. $O(\alpha_s)$ matrix elements with colour dipole radiation), labelled CDM. Note that all models, except for HERWIG, use the same LUND fragmentation scheme [22] for hadronization. For all distributions the MRSD0 [9] parton distributions were assumed for the proton.

In case of the parton shower approach, the amount and hardness of the gluon radiation depends sensitively on the virtuality of the parton before and after the quark-photon vertex. In ep scattering Q^2 or W^2 or some function of both can be chosen as the scale for the maximum of the allowed virtuality. In this experiment we have investigated for the first time the kinematic region where $< Q^2 > \approx 15$ GeV^2 and $< W^2 > \approx 10^4$ GeV^2, i.e. in which the two alternative scales are significantly different. Considerably more gluon radiation will result if the larger , W^2, is chosen. For comparison with data, we have chosen the scales Q^2, W^2 and an intermediate scale $W.Q$. Distributions for each of these cases are denoted with PS(Q^2), PS(W^2) and PS($W.Q$).

3.3 Energy Flow and $< p_T >$ versus x_F

General features of the observed hadronic final state are presented, always excluding the scattered electron. For this analysis only the low Q^2 data sample was used.

The flow of energy measured in the calorimeter transverse to the beam axis, E_T, is shown in Fig. 4a as a function of pseudorapidity $\eta = -\ln\tan\frac{\theta}{2}$. Here θ is the polar angle of the energy deposition. Fig. 4b shows the flow of E_T, measured with the calorimeter in the rapidity interval $-3 < \eta < 3$, as a function of ϕ. Here ϕ is the angle in the plane transverse to the beam direction between the scattered electron and the energy deposition. We observe the current jet as collimated energy flow balancing the p_T of the electron at $\phi = \pi$.

The most natural frame in which to study the hadronic final state is its centre of mass system (CMS). In this frame we define the z^* axis[1] as the direction of the exchanged virtual photon. In the naive quark parton model the current and target jet fragmentation regions then correspond to the $+z^*$ and $-z^*$ hemispheres. In the hadronic CMS the distribution of particle momenta transverse to the virtual photon direction as a function of Feynman-x, $x_F = 2p_z^*/W$, is particularly sensitive to different QCD models [13]. Fig. 5 displays the mean transverse momentum squared $< p_T^{*2} >$ of the charged particles as a function of x_F ("seagull" plot). Only charged tracks measured within the acceptance

[1]The transformed variables are denoted with a * as superscript.

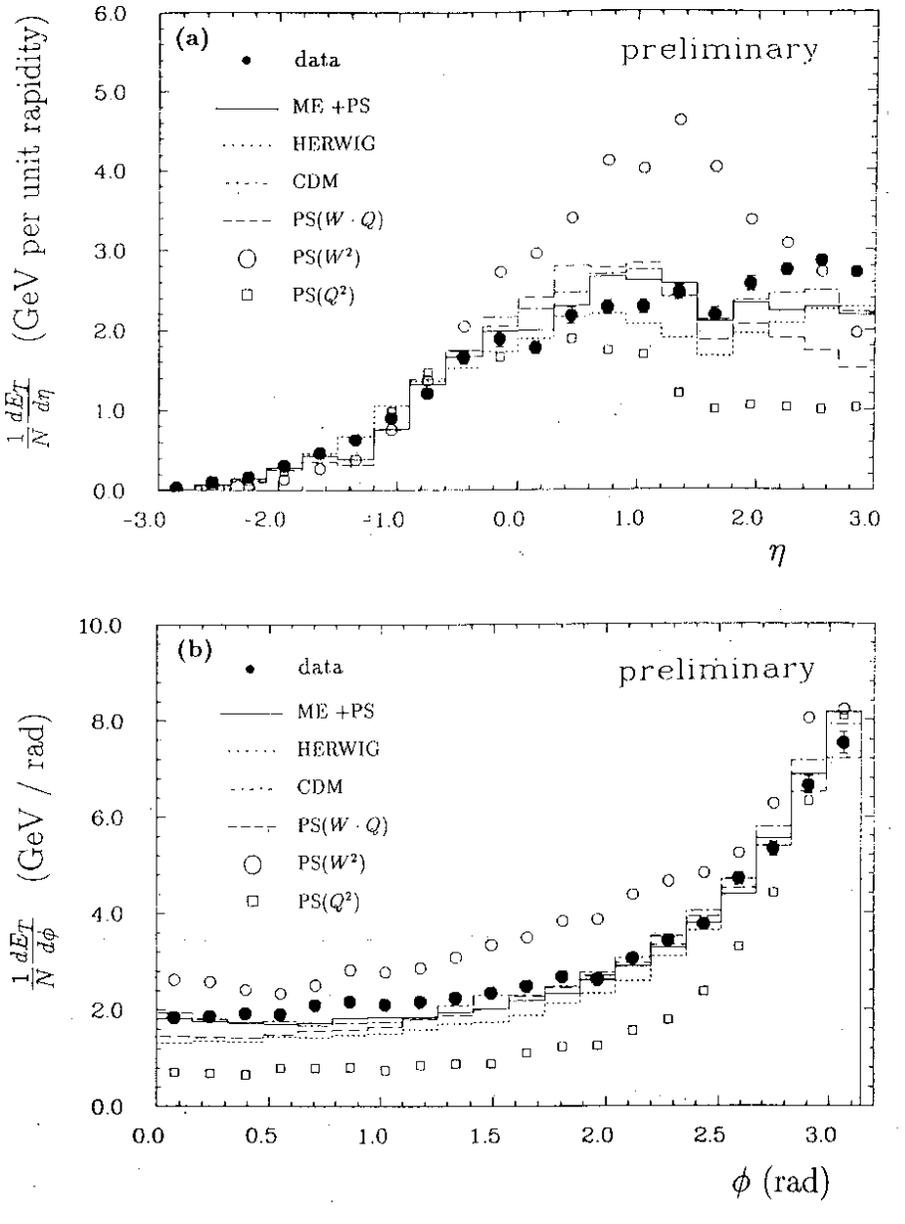

Figure 4: *Transverse energy flow E_T in the laboratory frame measured with the calorimeter* (a) *as a function of pseudorapidity η;* (b) *as a function of azimuthal angle ϕ with respect to the scattered electron direction in the plane transverse to the beam direction. The predictions of the different models are also given.*

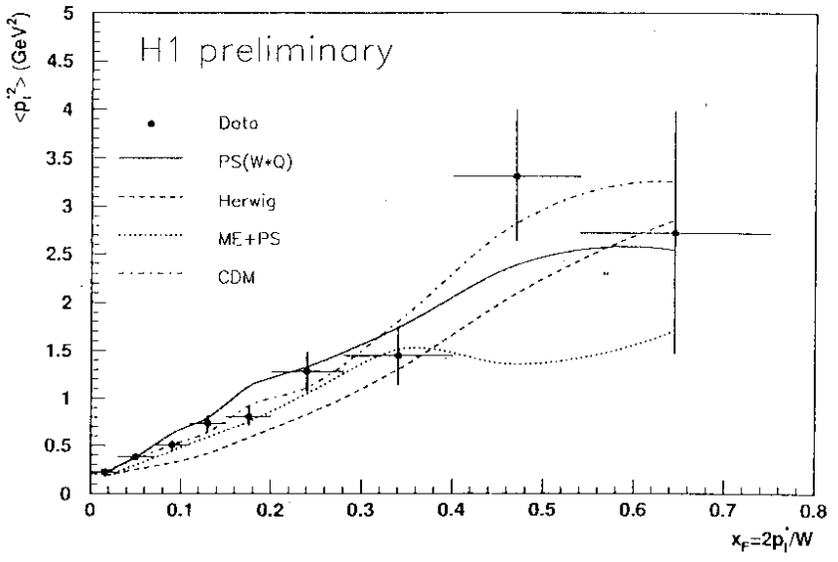

Figure 5: *Average p_T^{*2} as a function of x_F ("seagull" plot) for charged particles in the hadronic CMS. The model predictions are also shown.*

of the central tracker ($22^0 < \theta < 160^0, p_T > 0.1$GeV/c) have been used for this analysis. Due to this polar angle cut we are not sensitive to negative x_F.

Fig. 4 shows clearly that parton shower evolution with the large scale, PS(W^2), predicts too much transverse energy, and the evolution with the small scale, PS(Q^2), predicts too little. The same conclusion (see ref [16]) is obtained from the "seagull" plot analysis, where PS(W^2) is found to overestimate the average p_T^{*2} of the produced particles while PS(Q^2) underestimates it. Varying Λ_{QCD} between 10 and 800 MeV for PS(Q^2) and PS(W^2) does not lead to an adequate description of our data. The prediction of the simple quark parton model without QCD corrections is found to be similar to the PS(Q^2) model and can thus also be excluded. This is true even if we increase the parameter governing the p_T generated in the fragmentation process by a factor of 2. However, an intermediate scale, such as $W.Q$ describes reasonably the E_T flow spectra and seagull plot.

The HERWIG predictions (PS with Q^2 scale) give a reasonable description of the E_T flow and width of the current jet, but somewhat fail to describe the $< p_T^{*2} >$ versus x_F data, for $x_F < 0.3$.

Both the ME+PS and the CDM models are observed to describe the width of the current jet and the seagull data quite well and also give a reasonable description of the E_T distribution. All models tend to predict too little E_T in the forward region ($\eta > 2.0$) for the latter distribution. Detailed studies indicate that this is not the result of an insufficient understanding of the detector simulation in that region, but may hint to a poor description of the fragmentation of the proton remnant in the present models. Further study is necessary here.

In summary, the models based on first order matrix element calculations with additional parton shower evolution and on color dipole radiation are both able to reproduce the data at the present level of statistical sensitivity without any adjustment of parameters from values which describe parton processes in lower energy DIS data. The leading log parton shower approach with an intermediate scale, such as $W.Q$ is also compatible with our data.

3.4 Jet Rates

Quantitative studies of jet production have so far been carried out extensively in e^+e^- and $p\bar{p}$ collisions. Recently, first evidence for multi-jet structure in fixed target deep inelastic μN scattering was reported [14].

The event shown in Fig. 2 presents a 2+1 jet event in the H1 detector. Two well separated jets are visible in the energy flow plot, with a possible third jet close to the proton remnant direction. In the quark parton model (QPM), one jet arises from the struck quark scattering into the detector, while a second jet from the proton remnant generally escapes detection ("1+1" jet event configuration, Fig. 6a). Due to QCD processes to $O(\alpha_s)$, such as gluon radiation in the initial or final state (QCD Compton, Fig. 6b+c) or photon-gluon fusion (Fig. 6d), a further jet appears, giving rise to 2+1 jet events. The proton remnant is lost in the beam pipe. This is compensated in the jet algorithm by introducing a pseudoparticle carrying the missing longitudinal momentum of the event. In this analysis we make use of an (almost) Lorentz invariant cluster algorithm, referred to as the JADE algorithm [23]. In this scheme resolution (y_{cut}) dependent jet multiplicities are determined by calculating scaled invariant masses y_{ij} defined as

$$y_{ij} = \frac{m_{ij}^2}{W^2}, \qquad \text{with} \qquad m_{ij}^2 = 2E_iE_j(1-\cos\theta_{ij})$$

that is, neglecting the masses of cluster i and j. Here the invariant mass of the hadronic system W is chosen as a scale. Calorimeter cells are combined into clusters starting with the smallest invariant mass pair. Clustering is repeated until y_{ij} is above the jet resolution parameter y_{cut} for all clusters. The remaining clusters are counted as jets.

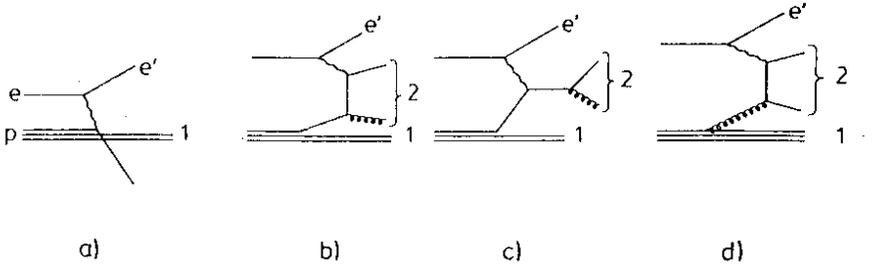

Figure 6: *Processes giving rise to 1+1* (a) *and 2+1* (b-d) *jet events in deep inelastic scattering.*

Jet reconstruction is based on calorimetric cells in the liquid argon and backward calorimeters which together cover a pseudorapidity interval of $-3.0 < \eta < 3.2$.

Fig. 7a and 7b show uncorrected data on fractional jet rates for 1+1, 2+1, and 3+1 jet events as a function of the jet resolution parameter y_{cut}, for the low and high Q^2 sample respectively. Fixing the jet resolution parameter at $y_{cut} = 0.02$ corresponding to $m_{ij} > 10 - 30$ GeV yields a 3 jet fraction of $R_{2+1} = 9\% \pm 1\%$ ($20\% \pm 6\%$) in the low (high) Q^2 sample respectively (statistical errors only). The ME+PS model describes the jet rates best, reproducing also the 4-jet rate. It has been checked that the jet rates at the level of partons, hadrons, and after detector simulation differ by less than 2% for jet resolutions $y_{cut} \geq 0.02$. HERWIG gives a fair description, however the 4-jet rate is not properly described. Both PS(WQ) and CDM predict too high multi-jet rates.

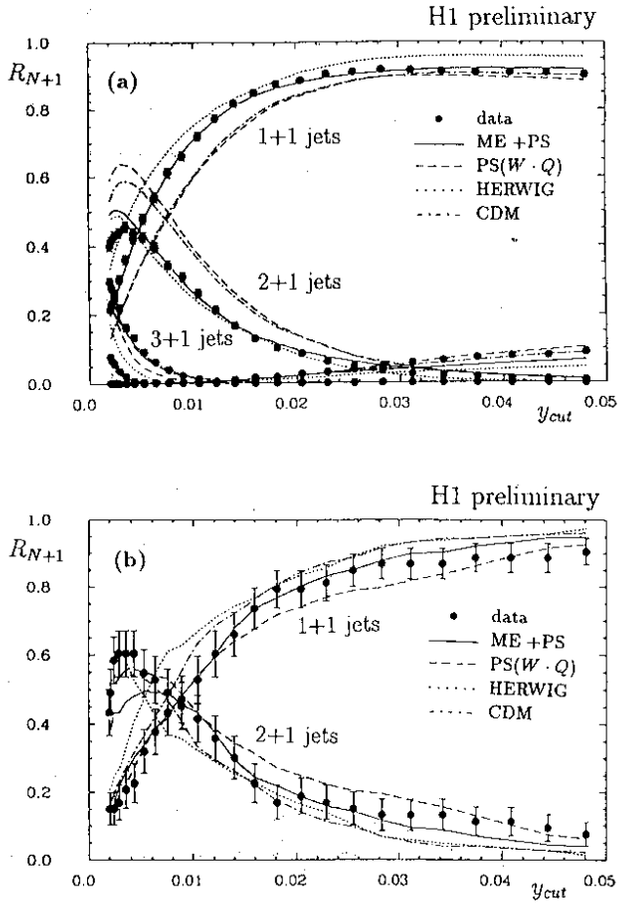

Figure 7: *Fractional jet rates versus the jet resolution parameter y_{cut} for* (a) *the low and* (b) *the high Q^2 event sample compared to the predictions of different QCD models.*

Fig. 8a shows the fractional 3-jet rate as a function of the momentum transfer Q^2. We observe the expected rise with Q^2 due to the increased phase space for multi-jet production. Both the ME+PS and the HERWIG model give a good description of the data, while PS(WQ) predicts a too high 3-jet rate and CDM fails to describe the rise with Q^2.

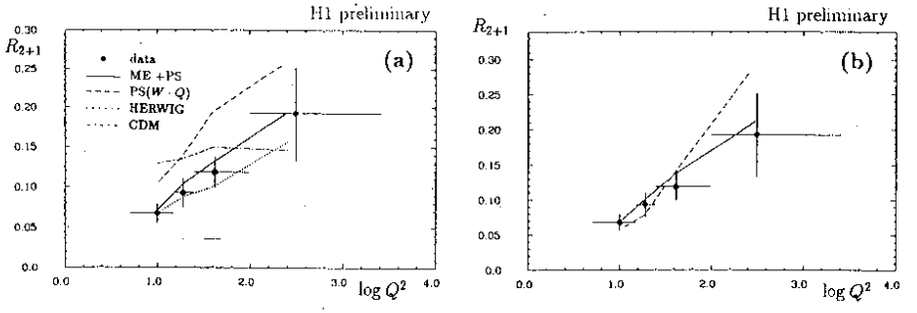

Figure 8: *3-jet rate versus momentum transfer Q^2* (a) *comparing different QCD model prediction and* (b) *comparing the ME+PS model with a running (solid line) and constant (dashed line) α_s.*

Since the rate of 3-jet events is proportional to α_s (c.f. Fig. 6b-d), the Q^2 dependence of the 3-jet rate is sensitive to the Q^2 variation of α_s. Fig. 8b shows the 3-jet rate as a function of Q^2 compared to the ME+PS model with a running α_s and a constant α_s. Although with the present data no discrimination is possible, it can be seen that the slope of the Q^2 variation of the 3-jet rate is sensitive to the running of α_s.

4 Proton Structure Function at Low x

One of the main physics topics at HERA is the exploration of the structure of the proton in the newly accessible Q^2 and x region. Precise QCD tests will be possible in the high Q^2 regime, but are at present hampered by the limited available statistics. With the present data we can study the low-x region down to values of 10^{-4}, while still staying in the DIS regime. At these low x values new QCD effects like saturation and gluon recombination could become visible. The present analysis measures for the first time the structure function $F_2(x, Q^2)$ in this small x region.

4.1 Parton Distributions at Low x

Structure function measurements are a key ingredient for the determination of parton distributions of nucleons. Precise knowledge of parton distributions is important e.g. for the calculation of production processes in hadronic interactions which can be described by perturbative QCD. Since future high energy colliders will be sensitive to x values of $O(10^{-3})$, measurements at HERA will be a key input for understanding the production rates. Moreover, the dynamics that generates parton distributions at low-x is a field of strong theoretical interest[24]. In particular, novel perturbative QCD effects are expected to show up at x values below 10^{-3}.

An overview of the present status of parton distribution parametrizations has been given by Martin in these proceedings [25]. The behaviour of the parton distributions at small values of x is presently dictated by the fixed target muon-proton experiments, which include measurements down to $x = 8.10^{-3}$. For smaller x values there is no direct guide from data, leaving room for theoretical speculation

on the behaviour of the parton distributions in this region[26]. In fact, extrapolations of presently proposed parton distributions in this range vary wildly. These extrapolations are often motivated by the following theoretical scenarios. On the one hand the evolution equations in perturbative QCD predict a fast growth of the gluon density $xG(x)$ in the proton, for small x. The linear evolution equation particularly adapted to study the small x region is the Kuraev-Fadin-Lipatov equation [27], which predicts a characteristic $x^{-\lambda}$ behaviour of the gluon density at small x, with $\lambda \sim 0.5$. It is however not clear at which x value the onset of the $x^{-0.5}$ behaviour should become visible. This result has to be contrasted with the expectations of the naive Regge-parton model where $xG(x) \sim x^{1-\alpha_{P(0)}}$, with the Pomeron intercept $\alpha_{P(0)} \simeq 1$, hence $xG(x) \sim$ constant.

At low x the sea quark distribution is driven by the gluon distribution, thus the $F_2(x,Q^2)$ evolution at small x is expected to reflect the assumptions made on $xG(x,Q^2)$. For example, assuming an $x^{-0.5}$ behaviour of the gluon density results in a rapid growth of $F_2(x,Q^2)$. Since $F_2(x,Q^2) \sim \sigma^{\gamma^*}_{tot}$ a continuing increase would lead to an unphysical blowup of the cross section. Therefore, at very small x the rise of the gluon density must be damped by a new mechanism. A proposed scenario is that at small x the parton densities become so large that annihilation and recombination of parton pairs will start to compete with the parton decay processes included in the standard evolution equations. Such "screening" or "shadowing" effects damp the fast increase of the parton density. It is however not possible to predict if HERA data will probe this region, since the onset of these effects depends strongly on the the rise of the gluon density at small x: an observed strong rise of $F_2(x,Q^2)$ would considerably enhance the probability of observing these novel effects at HERA!

We will compare presently available parton distributions which are in accord with the newly available NMC data [3], with our data. These are the MRSD[9], the CTEQ[28] and the GRV distributions[29]. The first two parametrizations use the same technique to derive parton distributions. The parton densities are parametrized for all x at one value of Q^2, e.g. $Q^2 = 4$ GeV^2. These parametrizations are evolved up in Q^2 using Altarelli-Parisi evolution equations[30], and fitted to all available x, Q^2 data. Often two or more parametrizations are proposed which include different assumptions on the gluon density in the unexplored small x region. For the MRSD distributions the small x evolution of the gluon density (at $Q_0^2 = 4$ GeV) is assumed to be singular, $x^{-0.5}$, for the MRSD– parametrization and constant for the MRSD0 parametrization. Similarly, for the CTEQ distributions the small x evolution of the gluon density is assumed to be singular, $x^{-0.5}$, for the CTEQ1MS parametrization and constant for the CTEQ1M parametrization. The GRV parametrization has a different starting point. Here it is assumed that at a very small Q^2 scale, namely $Q^2 = 0.3$ GeV^2, the quark and gluon distributions are "valence like", i.e. the parton densities vanish for $x \to 0$. The low x behaviour at larger Q^2 is dynamically generated by the evolution of the parton distributions, using the Altarelli-Parisi evolution equations. As a result the small x behaviour of the parton distributions is essentially fixed for the HERA range.

4.2 Event Selection and Background

With the available luminosity a meaningful structure function determination is limited to values of $Q^2 \leq 100$ GeV^2. Therefore we have restricted the analysis to those electrons which are scattered into the backward electromagnetic calorimeter (BEMC) at a polar angle of less than about 160°. Since the lever arm in Q^2 is rather limited, we present the $F_2(x,Q^2)$ measurement as function of x for given Q^2 values rather than as a function of Q^2 for given x values.

The trigger pertinent to this analysis required that there be a local energy deposit, or cluster, of larger than 4 GeV in the BEMC. The redundancy of the H1 trigger system allowed the determination of the efficiency of this trigger. It was found to be better than 99% for electron energies larger than 10 GeV. Events were rejected if signals in two adjacent scintillator planes (the Time-of-Flight System) behind the BEMC were compatible with particles produced in proton background interactions. Timing and offline analysis investigations determine the TOF efficiency for deep inelastic interactions to be $97 \pm 2\%$. The number of triggers recorded was about $5 \cdot 10^5$.

The current results were obtained by two independent analysis chains. In the first – termed analysis I – the event kinematics was calculated from the scattered electron variables E'_e and θ_e only, according to eqn. (2). The cross sections and related efficiencies were determined in $\sqrt{E'_e}, \theta_e$ bins which match the resolution and acceptance of the detector. The calculated cross sections in these detector oriented bins were then transformed to cross sections in x and Q^2. The kinematical region used in this analysis is $E'_e > 10.4$ GeV, $157.5 < \theta_e < 172.5$. In the second analysis – termed analysis II – bins in x, Q^2 were used for cross section and efficiency calculations. Information on both the scattered electron and hadronic final state was used to determine the event kinematics. The Q^2 value was determined from the electron variables only, using equation (2), but y was determined from the hadrons, using equation (3). The kinematical region used for this analysis was $\theta_e < 174^0, y_h < 0.5, E'_e > 10.6$ GeV and $\theta_{jet} > 30^0$

The two analyses differ further in the $\gamma - p$ background subtraction, usage of simulated data and electron identification. Analysis I and II use different parts of the detector to calculate the event kinematics and the necessary radiative corrections are quite different [31, 32]. The observed agreement between structure functions of both analyses represents therefore an important cross check of our measurements.

A sequence of cuts has been applied to isolate the genuine deep inelastic events for both analyses:

- An energy cluster of more than 7 GeV was required in the BEMC in association with a hit in the backward proportional chamber (BPC). Cluster size and cluster-track distance requirements were imposed in order to retain only events which have an electron candidate.
- A vertex, reconstructed from tracks found in the central tracker, inside ±50cm from the nominal interaction point was required. The vertex reconstruction efficiency was determined from the data to be about 90% at energies below the kinematic peak ($E'_e \leq 22$ GeV.). It drops to smaller values at larger energies since the backward scattered electron is accompanied by an energetic jet travelling at small angle which tends to be lost down the beam hole.
- The remaining beam-gas background of a few % was removed by using filters on the central tracking detector, suppressing events which had a large fraction of tracks pointing outside the interaction region.

A visual scan of a large fraction of the data suggests that the purity of the remaining *ep* interaction sample is larger than 98%. This result is confirmed by studies of the effect of the cuts described on the pilot bunch data sample. Pilot bunches do not have partners in the opposing beams with which they may collide. During the 1992 data taking period HERA provided 1 pilot bunch and 9 colliding bunches for each beam. No pilot bunch event survived the above cuts in the analysed kinematic region.

While the beam induced background has been removed there persists a noticeable background from photoproduction events at lower cluster energies ($E'_e \leq 14$ GeV). These are real *ep* collisions which involve a small Q^2 and thus the electron is scattered at a small angle and remains in the beampipe. Particles produced in the collision may fake an electron signal in the detector, which is then wrongly taken to be the scattered electron. No photoproduction rejection cuts were used for Fig. 1b, which shows the contribution of the background in the region $y > 0.6$. For analysis I, which uses a relatively loose electron identification cut, the photoproduction background was reduced by using the additional requirement $\sum_{all} E - p_z > 30$GeV. The residual contamination of photoproduction events in the data samples can be monitored with the small angle electron tagger installed 30 m downstream of the H1 main detector. The electron tagger detects about 10% of the electrons from photoproduction interactions which are scattered under small angles (for more details see [33], these proceedings) and allows the identification of photoproduction events. From electron tagger studies and extensive photoproduction Monte Carlo studies we conclude that the overall remaining photoproduction contamination is less than 2% and less than 10% for the lowest x datapoints presented here.

After all cuts about 1,000 events are left in the data samples used for analysis I and II. The efficiencies of the applied cuts have been determined from studies of the data. The total efficiency

for all cuts ranges between 50% and 60%. Acceptance and smearing corrections were determined from detailed simulation of large event samples, using different Monte Carlo generator programs and different assumptions for the a priori unknown structure function. The resulting differences in acceptance corrections were included in the systematic errors of the data points.

4.3 Differential Cross Sections and $F_2(x, Q^2)$

The cross sections determined from analysis I, not corrected for radiative events, are shown in Fig. 9, for constant values of θ_e.

In the Born approximation the deep inelastic scattering cross section at low Q^2 is determined by the two structure functions F_2 and $2xF_1 = F_2/(1+R)$:

$$\frac{d^2\sigma}{dxdQ^2} = \frac{2\pi\alpha^2}{Q^4 x}(2\,(1-y) \;+\; \frac{y^2}{1+R})F_2(x,Q^2). \qquad (4)$$

QCD gives a prescription for the calculation of $R(x,Q^2)$ for given parton distributions. E.g. assuming the MRSD0 (MRSD−) distributions one finds for $Q^2 = 15$ GeV^2, $R = 0.4$ ($R = 0.5$) at $y = 0.5$, and decreases with decreasing y. $R(x,Q^2)$ will be measured at HERA, but event samples corresponding to an integrated luminosity $\int Ldt \geq O(10pb^{-1})$ are needed. At present the extraction of $F_2(x,Q^2)$ requires that an assumption on the value of R be made. We have chosen the QCD prediction obtained using the MRSD− parton distributions. Note that R is only significant in the high y region, where it changes the cross section by about 8%.

Radiative corrections were applied using numerical calculations from the program TERAD91[32, 35] and the Monte Carlo program HERACLES[7] and FRANEQ[34] The result from TERAD91 is shown in Fig. 10. For the pure electron analysis the corrections are up to 20% (40%) for the lowest x points, assuming the MRSD− (MRSD0) parton distributions for the proton, while the corrections do not exceed 8% for the mixed electron-hadron analysis.

The measured $F_2(x,Q^2)$ is presented in Fig. 11 for two values of Q^2, 15 GeV^2 and 30 GeV^2. The results of analysis I "H1 electron" and of analysis II "H1 mixed" are found to be in excellent agreement. The calculation of the systematic uncertainty included the following error sources: possible shifts of the electron energy scale by 2% (15% at largest x; 2-3% elsewhere) and of θ_e by 5 mrad (4%); uncertainties in the detector efficiency calculations (5%); electron and proton beam induced background (4% for lowest x); photoproduction contamination in the lowest x bin (10%); the influence of different structure functions and hadronization uncertainties on the acceptance calculation (10% at most); the bin size correction (4%); radiative corrections (10% at lowest x for the electron method). Additionally, not shown, there is a global 12% normalization uncertainty on each data point, resulting from the uncertainty of the luminosity measurement and the remaining uncertainty on the efficiency of the time of flight scintillator cut and the z-vertex position requirement.

The large x data point "H1 norm" allows us to check our absolute normalization with respect to the existing lower energy muon proton data. For this data point the cross section was calculated in a wide x-bin, between $x \sim 5.10^{-3}$ and $x = 1$, dictated by the poor resolution at high x. We use the measured *shape* of the lower energy data to calculate the average x value of this bin. Fig 11. shows that the high x measurement is in agreement with the fixed target data from NMC[3], giving a cross check of the global normalization with an accuracy of ~20%.

At low x the $F_2(x,Q^2)$ is seen to rise with decreasing x. The extrapolations/predictions of different parton distributions are compared with the data. The GRV and MRSD− distributions are found to describe the data quite well, while the CTEQ and MRSD0 distributions are significantly below the data. For the GRV distribution the rise of the parton density at small x is generated dynamically, while for the MRSD− distribution a Lipatov $1/\sqrt{x}$ type of behaviour is assumed for the gluon at small x. The CTEQ1MS distribution assumes a Lipatov behaviour of the gluon too, but for this parametrization the sea quark distributions are not strongly coupled to the gluon distribution. As

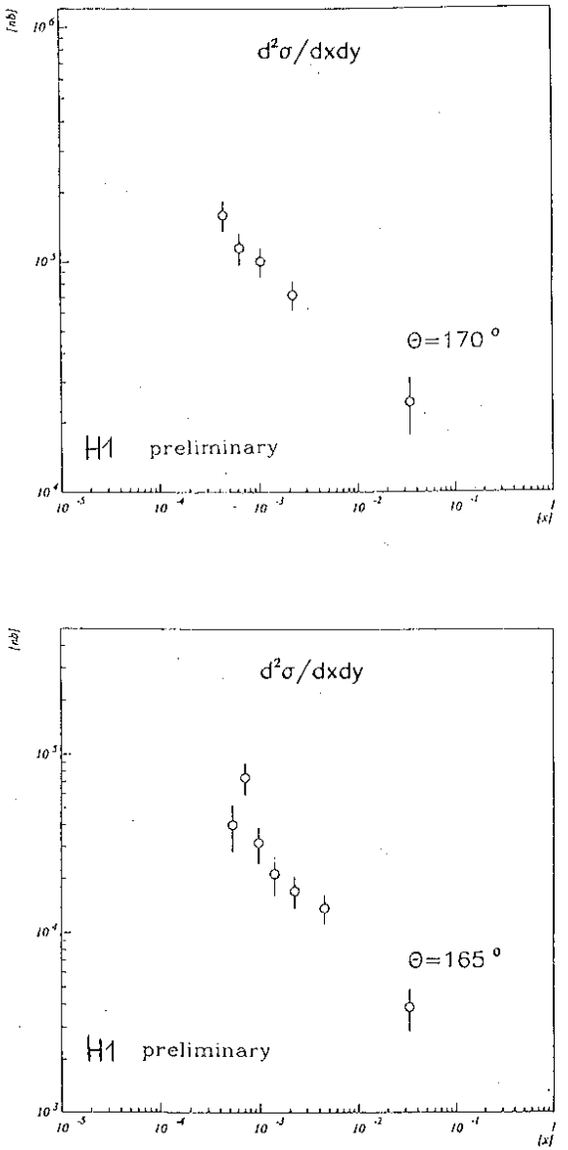

Figure 9: *The full differential cross section as function of x for constant θ_e. Statistical and systematical errors are added in quadrature. Additionally, all points are subject to a 12% normalization uncertainty, not shown in the figure.*

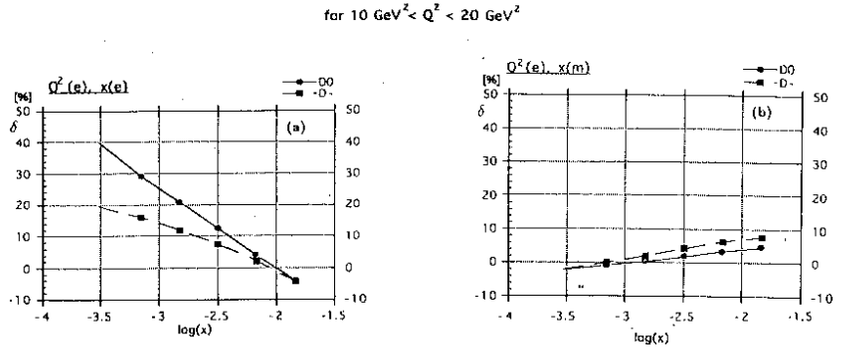

Figure 10: *Radiative corrections, $\delta = \sigma_{full}/\sigma_{Born} - 1$, for cross sections* (a) *determined with the electron variables and* (b) *determined with the hadron-electron mixed variables, for two different parton parametrizations MRSD0 and MRSD−.*

it turns out the predicted sea quark distribution at small x is rather flat and hence the resulting $F_2(x, Q^2)$ is not very different from the CTEQ1M and MRSD0 predictions.

It is tempting to conclude that the measurements of $F_2(x, Q^2)$ indicate the observation of the Lipatov behaviour at small x. However, to establish this unambiguously a careful analysis of the $F_2(x, Q^2)$ evolution at different Q^2 values with more precise data needs to be made. Additional information, e.g. from DIS events with associated high x jets will be needed to establish or support this picture. It is in any case encouraging to see $F_2(x, Q^2)$ rise at small x, since this means that the parton saturation regime can be reached earlier, possibly already at HERA at somewhat smaller x values than presented in this analysis. The result suggests that there is much exciting physics to be done at HERA; we are eagerly awaiting more data.

5 Conclusion

New results on the hadronic final state and proton structure function $F_2(x, Q^2)$ measurements in electron proton deep inelastic scattering events at HERA were presented by the H1 experiment. Global event characterisitics and jet rates have been studied. The data can well be described by models based on $O(\alpha_s)$ matrix elements with matched parton showers. The first, preliminary, measurements of $F_2(x, Q^2)$ show a rise of $F_2(x, Q^2)$ with decreasing x.

6 Acknowledgements

I am very grateful to all my colleagues of the H1 DIS analysis groups for their effort in getting these results. I thank in particular M. Klein, M. Krasny, E. Peppel, H. Kuester, M. Kuhlen, A. Wegener and R. Nisius for valuable discussions

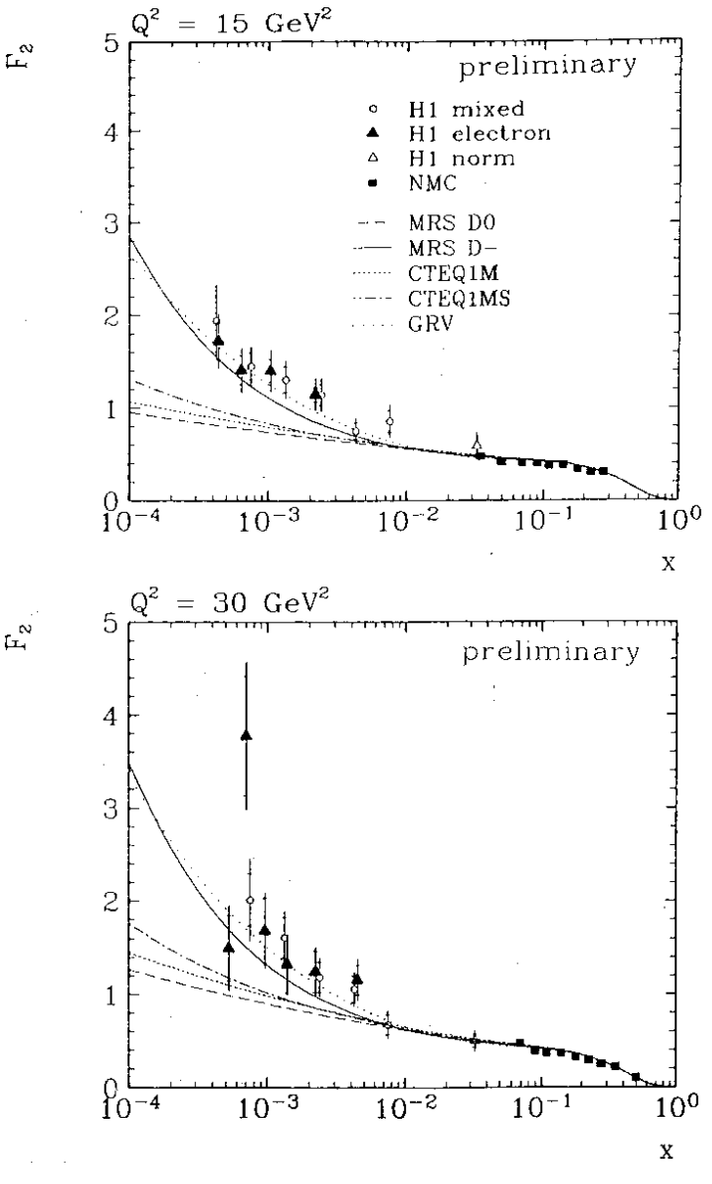

Figure 11: *The structure function $F_2(x, Q^2)$ for 2 values of Q^2, compared to previous experimental results and parton parametrizations (described in the text). The inner error bars indicate the statistical errors, the full error bars are the statistical and systematic errors added in quadrature. Additionally, all points are subject to a 12% normalization uncertainty, not shown in the figure.*

References

[1] M. Breidenbach et al., Phys. Rev. Lett. **23** (1969) 935.

[2] J. Feltesse, Proceedings of the Lepton Photon Conference 1989, SLAC, ed. M. Riordan, (1989) 13 and references therein.

[3] NMC Collab., P. Amaudruz et al., Phys. Lett. **295B** (1992) 159.

[4] F. Brasse, *The H1 Detector at HERA*, to appear in: Proceedings of the 26th International Conference on High Energy Physics, Dallas (1992) and DESY preprint 92-140 (1992);
H1 Collab., *The H1 Detector at HERA* to be submitted to Nuclear Instruments & Methods.

[5] A. Blondel and F. Jacquet, Proceedings of the Study of an *ep* Facility for Europe, ed. U. Amaldi, *DESY* **79-48** (1979) 391.

[6] H1 Collab., T. Ahmed et al., Phys. Lett. **299B** (1993) 374.

[7] A. Kwiatkowski, H. Spiesberger, and H.-J. Möhring, Comp. Phys. Commun. **69** (1992) 155, and references therein.

[8] G. Ingelman, "LEPTO 5.2", unpublished program manual;
H. Bengtsson, G. Ingelman, and T. Sjöstrand, Nucl. Phys. **B301** (1988) 554.

[9] A. D. Martin, W. J. Stirling, R. G. Roberts, Phys. Rev. **D47** (1993) 867.

[10] S. Bentvelsen, P. Kooijman and J. Engelen, Proceedings of the Workshop "Physics at HERA", ed. W. Buchmüller and G. Ingelman, Hamburg (1992) 23;
K.C. Hoeger, Proceedings of the Workshop "Physics at HERA", ed. W. Buchmüller and G. Ingelman, Hamburg (1992) 43.

[11] J. Gayler, to be published in the Proceedings of the 3rd Int. Conf. on Calorimetry in High Energy Physics, Corpus Christi (1992).

[12] EMC Collab., J.J. Aubert et al., Phys. Lett. **95B** (1980) 306, Phys. Lett. **100B** (1981) 433, Phys. Lett. **119B** (1982) 233.

[13] EMC Collab., M. Arneodo et al., Z. Phys. **C36** (1987) 527.

[14] E665 Collab., M.R. Adams et al. Phys. Rev. Lett. **69** (1992) 1026.

[15] B. Andersson et al. Z. Phys. **C9** (1981) 233,
G. Ingelman et al. Nucl. Phys. **B206** (1982) 239.

[16] H1 Collab., T. Ahmed et al., Phys. Lett. **298B** (1993) 469.

[17] H. Küster, *Jets in Deep Inelastic Scattering at HERA* to appear in the proceedings of the 28th Rencontre de Moriond, March (1993).

[18] S. Magill, these proceedings;
ZEUS Collab., M. Derrick et al., DESY preprint 93-30.

[19] G. Marchesini et al., Comp. Phys. Comm. **67** (1992) 465, and references therein.

[20] G. Ingelman, "LEPTO 6.1", Proceedings of the Workshop "Physics at HERA", ed. W. Buchmüller and G. Ingelman, Hamburg, (1992), 1366, and references therein.

[21] L. Lönnblad, ARIADNE version 4.03, Comp. Phys. Commun. **71** (1992) 15, and references therein.

[22] T. Sjöstrand, Comp. Phys. Commun. **39** (1986) 347;
T. Sjöstrand and M. Bengtsson, Comp. Phys. Commun. **43** (1987) 367, and for JETSET 7.3, CERN-TH. 6488/92 (1992).

[23] JADE Collab., W. Bartel et al. Z. Phys. **C33** (1986) 23.

[24] A.H. Mueller, these proceedings; J. Kwiecinski these proceedings; E. Levin, these proceedings.

[25] A.D. Martin, these proceedings; A.D. Martin, W.J. Stirling and R.G. Roberts, Durham preprint, DTP-93-22, Rutherford preprint RAL 93-027 (1993).

[26] J.Bartels and J.Feltesse, Proceedings of the Workshop "Physics at HERA", ed. W. Buchmüller and G. Ingelman, Hamburg (1992) 133 and references therein;
Workshop on Deep Inelastic Scattering, April 1992, Teupitz, Germany, J. Blümlein and T. Riemann editors.

[27] E.A. Kuraev, L.N. Lipatov and V.S. Fadin, Phys. Lett. **60B** (1975) 50; Zh.E.T.F **72** (1977) 377.

[28] J. Botts et al., Phys. Lett. **304B** (1993) 159.

[29] M. Glück, E. Reya and A. Vogt, Z. Phys. **C53** (1992) 127;
M. Glück, E. Reya and A. Vogt, Phys. Lett. **306B** (1993) 391.

[30] G. Altarelli, G. Parisi, Nucl. Phys. **126** (1977) 297.

[31] J. Blümlein, Phys. Lett. **271B** (1991) 267.

[32] A. Akhundov et al., Proc. Workshop "Physics at HERA", ed. W. Buchmüller and G. Ingelman, Hamburg, (1991) 1285.

[33] G. Knies, these proceedings.

[34] W. Placzek, Proceedings of the Workshop "Physics at HERA", ed. W. Buchmüller and G. Ingelman, Hamburg, (1991) 1433.

[35] A. Akhundov, contributed paper to the XXI International Meeting on Fundamental Physics, "Physics at HERA", Madrid, 1993.